Carrier dynamics in polymer nanofiber : fullerene solar cells

Kurniawan, Michael; Salim, Teddy; Tai, Kong Fai; Sun, Shuangyong; Sie, Edbert Jarvis; Wu, Xiangyang; Yeow, Edwin Kok Lee; Huan, Alfred Cheng Hon; Lam, Yeng Ming; Sum, Tze Chien

2012

Kurniawan, M., Salim, T., Tai, K. F., Sun, S., Sie, E. J., Wu, X., et al. (2012). Carrier dynamics in polymer nanofiber : fullerene solar cells. Journal of Physical Chemistry C, 116(34), 18015–18022.

https://hdl.handle.net/10356/94929

https://doi.org/10.1021/jp302968e

THE JOURNAL OF PHYSICAL CHEMISTRY C

NANYANG TECHNOLOGICAL UNIVERSITY

Subscriber access provided by Nanyang Technological Univ

Article

Carrier Dynamics in Polymer-Nanofiber:Fullerene Solar Cells

Michael Kurniawan, Teddy Salim, Kong Fai Tai, Shuangyong Sun, Edbert Jarvis Sie, Xiangyang Wu, Edwin Kok Lee Yeow, Cheng Hon Alfred Huan, Yeng Ming Lam, and Tze Chien Sum

J. Phys. Chem. C, **Just Accepted Manuscript** • DOI: 10.1021/jp302968e • Publication Date (Web): 04 Aug 2012

Carrier Dynamics in Polymer-Nanofiber:Fullerene Solar Cells

Michael Kurniawan [a], Teddy Salim [b], Kong Fai Tai [a], Shuangyong Sun [b], Edbert Jarvis Sie [a], Xiangyang Wu [c], Edwin Kok Lee Yeow [c], Cheng Hon Alfred Huan [a], Yeng Ming Lam [b] and Tze Chien Sum [a*]

[a] Division of Physics and Applied Physics, School of Physical and Mathematical Sciences, Nanyang Technological University, 21 Nanyang Link, 637371, Singapore;

[b] School of Materials Science and Engineering, Nanyang Technological University, 50 Nanyang Avenue, 639798, Singapore

[c] Division of Chemistry and Biological Chemistry, School of Physical and Mathematical Sciences, Nanyang Technological University, 21 Nanyang Link, 637371, Singapore

RECEIVED DATE (to be automatically inserted)

*Corresponding author; tzechien@ntu.edu.sg

ABSTRACT:

Organic photovoltaic (OPV) devices fabricated with P3HT nanofiber (NF) networks typically exhibit poorer device performance compared to their nanoscale phase separated P3HT:PCBM counterparts despite possessing superior light harvesting properties and high in-plane charge mobility. Herein, we investigate the charge generation and recombination dynamics in P3HT-NF:PCBM blend films using transient absorption spectroscopy (TAS) spanning a wide temporal range over 7 orders of magnitude (i.e. from 100 fs to 1 μs), which are correlated with device performance studies. TAS reveals a more efficient charge generation and polaron formation rate in the NF samples as compared to the control samples at the onset which persists up to ~2 ns. However, within the ns to μs timescale, there is a significant amount of non-geminate recombination in the NF system. We attribute this to the poor inter-fibrillar charge transport between the NFs, which tend to align parallel to the electrodes, thereby causing charge localization. These charge dynamics were validated using the analytical model proposed by Laquai and co-workers (Howard, I. A. *et. al.*, J. Am. Chem. Soc. 2010, 132 14866). Importantly, our findings provide new insights into the factors that limit the photovoltaic performance of such P3HT-NF based devices.

KEYWORDS: photovoltaic device, thiophene polymer, nanofibers, morphology, transient optical spectroscopy, and charge dynamics

1. Introduction

Organic photovoltaic (OPV) devices[1-6] present a promising solution to our clean and renewable energy needs and within the last decade, great inroads have been made in their development. Key advantages of OPV devices over their inorganic counterparts include: easy processability; large scale and high throughput fabrication; and compatibility with low-temperature processes. One system that has received much attention is the poly (3-hexylthiophene):phenyl-C_{61}-butyric acid methyl ester (i.e. P3HT:PCBM) bulk heterojunction (BH) organic photovoltaic (OPV) system, which has demonstrated power conversion efficiencies (PCE) as high as 5%[7-10]. The high efficiency of the P3HT:PCBM system stems from the interpenetrating network of P3HT and PCBM-rich domains (formed by thermal annealing at elevated temperatures) and the increased molecular order essential for the transport of the excited species to the donor/acceptor (D/A) interfaces for dissociation into free carriers. These highly ordered although percolated pathways allow a more efficient charge transport to the electrodes following the charge dissociation[11]. Optimal PV device performance is achieved with domain sizes that are comparable to the exciton diffusion length (i.e. between 10-20 nm)[12-14]. Other methods to control P3HT:PCBM phase distribution include: solvent annealing[13,15], ordered templates (using anodic aluminum oxide template)[16], self-assembly with marginal solvents[17-19], etc.

Recent studies on the blend film morphologies of P3HT:PCBM have revealed the co-existence of three characteristic phases: fibrillar networks with widths of <20 nm, ordered aggregates and disordered matrices[20,21]. One exciting possibility to enhance the bulk heterojunction P3HT device performance is through the use of fibrillar networks. It has been shown that using a concentrated solution, the P3HT polymer phase can be pre-assembled under some specific conditions in solution to form predominantly P3HT-nanofibers (NFs) of dimensionality: diameter ~20 nm and length of a few microns. With enhanced absorbance[22-24], these highly crystalline, interconnected P3HT-NF networks

could function as light harvesting "antennae" in an OPV device. Other advantages include its excellent in-plane charge carrier mobility (0.3 cm^2/Vs) and thermal-free post-fabrication processing compatible with plastic substrates[21,25]. In a P3HT-NF:PCBM blend, the PCBM-rich phase would segregate around the NFs, filling up the complementary space in an interconnected P3HT fibrillar network. Specifically, the width/diameter of the NFs is comparable to the exciton diffusion length essential for efficient exciton harvesting laterally; while orthogonally, the highly-ordered π-π stacking along the NF length facilitates the efficient intra-fibrillar charge transport to other parts of the interconnected network following charge separation. Such P3HT-NF system with enhanced absorbance could simultaneously fulfill the criteria for efficient charge dissociation laterally along the entire length of the fiber) and efficient charge transport longitudinally along the fiber to the interconnected fibrillar network and subsequently to the electrodes. These salient properties of the P3HT-NF system are highly attractive for enhancing the performance of P3HT:PCBM OPV devices.

Despite the potential of the P3HT-NF system, devices fabricated with predominantly P3HT nanofibrillar networks typically exhibit lower PCE than those fabricated with their nanoscale phase separated counterparts[19,22]. Presently, systematic studies on the photophysics of P3HT fibrillar networks are still lacking. To optimize the material properties and device architectures of P3HT-NF based PV devices for higher efficiencies, it is imperative to gain a clear understanding of the fundamental photophysical processes governing charge generation, recombination, transport and extraction in P3HT NFs and correlate the relevance of these fundamental processes to the device performance of the OPV cell. For example, the short circuit current (J_{SC}), a key parameter of an OPV device performance, is dependent on the generation and dissociation of excitons at the D/A interfaces and the subsequent transport of free carriers to the electrodes. Importantly, these samples of highly ordered, interconnected P3HT fibrillar network allow us to investigate the dependence of the charge generation and

recombination dynamics in the P3HT:PCBM system on a crystalline order over much longer length scales than previously possible whilst not compromising the exciton harvesting criteria. Investigating the dynamics of the charge generation and recombination in these highly ordered, interconnected P3HT fibrillar networks and elucidating the origins of its poorer device performance are the main foci of this paper.

Herein, we report on a comprehensive optical spectroscopy study on the charge carrier dynamics in P3HT/PCBM films with different degrees of crystallinity/molecular ordering: i.e. non-annealed P3HT (NA P3HT), thermal annealed P3HT (TA P3HT), and the nano-fiber P3HT (NF P3HT); where the last sample was not subjected to any post-fabrication thermal processing as we intend to focus on this salient thermal-free post-fabrication possessing property of the NF system in this comparative study. Transient optical probes spanning the temporal regimes of charge generation, recombination, transport and extraction (i.e. over 7 orders of magnitude from 100 fs to 1 μs) were used in this study. These findings were correlated with the device performance studies of these samples. Femtosecond transient absorption spectroscopy reveals a more pronounced ground state bleach signature persisting up to 2 ns in the P3HT-NF:PCBM (NF Blend) system than that of the control (i.e. the thermal-annealed P3HT:PCBM (TA Blend) system); suggesting a higher rate of charge generation and polaron formation in the NF system. These transient dynamics were further analyzed within the framework of an analytical model proposed by Laquai and co-workers[19] where the branching ratios of geminate versus non-geminate recombination (i.e. equivalent to the branching ratio for the formation of charge transfer states versus ultrafast free charge generation) for the NF Blend and the TA Blend were determined to be approximately 0.09:0.91 and 0.14:0.86 respectively; thereby validating our findings of a more efficient charge generation and polaron formation rate in the NF system. However, there is also a significant amount of non-geminate recombination in the NF system over the timescale spanning hundreds of ns. We attribute this to the

poor inter-fibrillar transport between NFs lying parallel to the electrodes, which cause charge localization. Essentially, the interconnected P3HT fibrillar network is still a 2-D network with poor charge mobility orthogonal to the planar network. The higher carrier concentrations present result in: (a) an increased bimolecular recombination that competes with the charge extraction; and (b) a redistribution of local electric fields that inhibits the charge extraction. These effects are manifested in the lower J_{SC} and FF values of the NF Blend devices compared to the control TA Blend devices.

2. Experimental Methods

2.1 Materials and Sample Preparation

Regio-regular (RR)-P3HT NF (7 mg/ml) in *p*-xylene was prepared as follows: the mixture was first heated to 80^{o}C to ensure complete dissolution of the polymer before being gradually cooled back to room temperature at a rate of -10^{o}C/hr (Julabo F25-EC). The suspension was left undisturbed in the dark for 48 hrs to promote self-assembly of the P3HT NFs. Subsequently, this agglomeration was mixed with PCBM (to form the NF Blend) with a weight ratio of 10:8 and was thoroughly stirred without heating for 2 h before spin-coating. For comparison, the non-fiber blend (i.e. NA & TA Blend) was prepared by mixing RR-P3HT (10 mg/ml) with PCBM with the same weight ratio (i.e. 10:8) in 1, 2-dichlorobenzene (*o*-DCB).

2.2 Steady-State Absorption and Morphology Measurements

Steady-state absorption spectra were recorded using a UV-VIS absorption spectrometer (Jasco Spectrometer V-650) and tapping mode atomic force microscope (AFM – Veeco di Dimension D3100V) was used to image the surface morphology of the polymer films.

2.3 Transient Absorption Spectroscopy

Transient absorption spectroscopy (TAS) was performed using two different experimental setups – one for the fs–ns temporal regime (i.e. femtosecond transient absorption spectroscopy (fs-TAS)) and the other for the ns–μs temporal regime (i.e. ns laser flash photolysis spectroscopy). For the TAS measurements, thin films (~100 nm) of the polymers (i.e. P3HT-only films, including both the NF and the non-fiber control) and their respective blends were spincoated on pre-cleaned quartz substrates. No thermal annealing was performed on the NF P3HT & NF Blend samples after the spin coating. Extreme care was taken to ensure that the incident laser pump fluence, beam spot size, the overlap of pump and probe beam, as well as the film thicknesses are comparable – this is to ensure that the excitation densities used were kept equal.

2.3.1 Femtosecond Transient Absorption Spectroscopy (fs-TAS)

fs-TAS was performed in a non-degenerate pump-probe configuration where the excitation pulses were generated from an optical parametric amplifier (OPA – Light Conversion TOPAS^{TM}) that was pumped by a 1 kHz regenerative amplifier (i.e. Coherent Legend^{TM}; center wavelength: 800 nm; pulse width: 150 fs; power: 1 mJ/pulse), which was seeded by an 80 MHz Coherent Vitesse^{TM} oscillator. The 500 nm pump pulses from the OPA were focused onto a 200 μm^2 spot and overlapped with white-light continuum (i.e. 450 – 780 nm) probe pulses generated with a thin sapphire plate using 800 nm laser pulses. Pump-induced changes of the probe beam transmittance (ΔT/T) through the sample were monitored using a monochromator/PMT configuration with lock-in detection. The pump beam was chopped at 83 Hz and this was used as the reference frequency for the lock-in amplifier. The pump fluence was kept to a minimal of 10 μJ/cm^2 per pulse to mimic a low intensity regime comparable to that for OPV operation in order to avoid any second order effects[26-28].

2.3.2 Nanosecond Transient Absorption Spectroscopy (ns-TAS)

ns-TAS was performed using a laser flash photolysis spectrometer (Applied Photophysics LKS.60 Nanosecond Laser Flash Photolysis Spectrometer). The excitation pulses are from a Nd:YAG, Q-switched laser (532 nm, 7 ns pulse width) and the probe is a 150 W Xe lamp aligned normal to the excitation source (i.e. Applied Photophysics LKS.60 Nanosecond Laser Flash Photolysis Spectrometer). Each time-resolved trace was acquired by averaging 100 laser shots at a repetition rate of 1 Hz with a R928 photomultiplier. The data was collected in reflection geometry with the sample positioned at 45^{o} with respect to both the excitation source and probe light.

2.4 Device Fabrication

The OPV devices were prepared on ITO-coated glass substrates (Kintec Company, 7 Ω/sq) with the following structure: ITO/PEDOT:PSS/P3HT:PCBM/Al. The substrates were successively ultrasonicated in deionized water, acetone and isopropanol for 15 mins each. They were subsequently blown dry with N_2 and then subjected to plasma-cleaning for 2 min. A thin PEDOT:PSS layer (~30 nm) was spin-coated onto the clean substrates at 3000 rpm for 60 s, followed by baking in a N_2 glovebox at 140^{o}C for 10 min. The NF Blend was spin-coated at 900 rpm for 90 s, while the non-fiber blend was spin-coated at 700 rpm for 120 s in order to achieve films of the same thicknesses. No filtration was performed for the NF Blend, while the non-fiber blend was filtered with a 0.2 μm PTFE filter. An Al layer of ~100 nm thickness was then deposited on these samples in the evaporator chamber ($<10^{-5}$ Pa). Following Al deposition, the TA Blend devices were thermally annealed at 150^{o}C for 30 min while there was no thermal treatment for the NF Blend devices. The current density-voltage (*J*-V) characteristics were measured under AM 1.5 G illumination (SAN-EI Electric) calibrated at 100 mW/cm^2 with a

semiconductor parameter analyzer (Agilent 4155-C). The calculated power conversion efficiencies were not corrected for spectral mismatch. External quantum efficiency (EQE) measurements were performed with a Merlin radiometer (Newport) and a calibrated Si-photodiode (Hamamatsu) was used as a reference device to count the incident photons.

3. Results and Discussions

3.1 Linear Absorption and Morphology Measurements

Fig. 1 shows the normalized linear absorption spectra of the various films of equivalent thicknesses. Structured peaks, indicative of the increased crystallinity and ordering in the P3HT system, are present in the NF Blend (non-annealed) sample and the TA Blend sample. The vibronic peaks at 510 nm, 560 nm and 600 nm, correspond to the 0-2, 0-1 and 0-0 absorption transitions of P3HT, respectively. The origins of these vibronic peaks and their relationship with the degree of crystallinity of the polymer have been investigated in detail by Spano *et. al.*[29,30]. Comparatively, these peaks are more pronounced and better resolved in the NF Blend samples than the other samples especially the prominent 0-0 ground state absorption peak at 600 nm. The strongest light absorbance of the NF Blend is consistent with an earlier report of the higher degree of ordering in the P3HT-NF system[25].

The difference in the morphology between the NF and non-NF Blend system is also evident from the AFM images (see Fig. 2) where distinct differences in the phase separation in the pristine P3HT:PCBM (Fig. 2(b)) and the NF Blend (Fig. 2(f)) can be clearly seen. Clear fibrillar structures with lengths ~1 μm are observed in the phase image of the NF Blend films, indicating that the fibrillar phase is predominant. Signatures of phase separation are also evident in the pristine P3HT:PCBM sample because of solvent annealing arising from the use of 1,2-dichlorobenzene (boiling point: 180.5 ^{o}C). The root-mean square (RMS) roughness of the pristine, TA Blend, and NF Blend films were found to be

approximately 0.3 nm, 0.8 nm, and 1.8 nm, respectively over a scan area of 1 μm^2. The higher RMS roughness of the NF Blend is in agreement with an earlier study[19].

3.2 Charge Carrier Dynamics in the fs-ns Temporal Regime

3.2.1 P3HT-only Films

fs-TAS was first performed on 100 nm thick P3HT-only films to understand the dependence of the charge generation and recombination dynamics on the extended crystalline order in the absence of the acceptor material. In view of the effect of solvent annealing in the pristine films giving rise to some degree of ordering in those films, it would be fairer to compare the dynamics from the ordered films only (i.e. the non-fiber TA P3HT control and the predominant NF P3HT sample). Fig. 3(a) shows the representative differential transmission (DT) spectra of the NF P3HT, where the three vibronic peaks corresponding to the 0-0, 0-1 and 0-2 absorption transitions (in the spectral region of 500 – 620 nm), manifest as pronounced ground state bleaching (GSB) signatures. This photobleaching (PB) signal (i.e. $\Delta T/T > 0$ – increased transmittance of the probe beam) arises due to the state-filling of the excitonic and polaronic states, which is proportional to the population of the excitons and polarons in the photoexcited films as previously validated by Guo *et. al.*[11] Monitoring the transient dynamics of the GSB bands would allow us to trace the evolution of these photoexcited species; while observing the relative magnitudes of the DT signal obtained from samples with equivalent thicknesses (of ~100 nm) would allow us to compare the relative populations of the residual excited species at different times following photoexcitation. The negative $\Delta T/T$ signal at 650 nm has previously been attributed to the photo-induced absorption (PIA) of these photogenerated charges[27]. The spectral profile of the NF P3HT film is similar to that of the TA P3HT (spectra not shown – see supporting information), except for the absence of the weak positive PB peak near 730 nm that would arise from the stimulated emission (SE) of singlet

excitons. It is likely that the stronger PIA signal in the P3HT-NF system may have overwhelmed the overlapping SE signal.

The GSB spectral profiles of both the TA P3HT control and the NF P3HT films are very similar. At early times, the magnitude of the DT signal for the 0-0 and 0-1 bands are more pronounced in the NF P3HT films than the TA P3HT (for 0-1 GSB signal, see Fig. S1 of Supporting Information). For the 0-0 transition, this is ~1.65 times larger at the 1 ps onset. This increased PB signal stems from the increased absorbance in the P3HT-NF films that yields a larger population of photogenerated excitons and polarons (i.e. ~65% more photoexcited species being formed at the onset). The decay profiles of the 0-2 bands of both samples are rather similar, indicating a comparable rate of depopulation of the 0-2 state to the lower excited states (i.e. 0-1 and 0-0) in both samples (see Fig. S1 of Supporting Information). In the absence of acceptor molecules (i.e. PCBM), charge transfer would be significantly suppressed in this donor-only system. Hence, the decay of the GSB bands (with lifetime τ ~ 50 ps) corresponds to the recombination of P3HT singlet excitons[27]. At around 100 ps, the magnitude of the 0-0 decay for both the NF P3HT and the TA P3HT films becomes comparable but does not recover back to the equilibrium. This prolonged PB (i.e. non-recovery of the PB signal to the equilibrium) beyond a 2 ns timescale is attributed to the long-lived hole polaron states, indicating that a small fraction of P3HT molecules remain in the excited state. Triplet formation is negligible due to the small intersystem crossing rate[26,31,32]. At 2 ns delay, the magnitude and the spectral profile of the GSB for both the TA P3HT and NF P3HT films are very similar, indicating that there are a comparable number of charges left in both systems. Over the 1 ps to 2 ns time scale, the temporal profiles of the GSB peaks in both systems are observed to be only slightly red-shifted by ~0.02 eV – see Fig. 3(a). This spectral shift has previously been attributed to the migration of the excitons and hole polarons to the lower energy crystalline regions (i.e. the more ordered regions) and their corresponding relaxation within the density of states[27]. This

small spectral shift also reflects a narrow density of states for the photoexcited species, implying that charge trapping due to defects would not be significant in both these ordered P3HT systems[33]. The relative prominence of the 0-0 peak at 2 ns compared to the other peaks in the GSB band further suggests that most of these long-lived charges are present in the more crystalline regions of the film. With the validation of the transient dynamics from the P3HT-only films with those reported in the literature and a comparison of the transient signatures for the NF P3HT and the TA P3HT films, we shall next turn our attention to the P3HT:PCBM blend films, which is the main focus of this work.

3.2.2 P3HT:PCBM Blend Films

A P3HT:PCBM ratio = 1:0.8 was used to prepare these 100 nm thick blend films. Fig. 4(a) shows the representative DT spectra of the NF Blend which is similar to those of the TA Blend (see supporting information). With the incorporation of PCBM in the P3HT films, electron transfer occurs almost instantaneously from the donor (P3HT) to the neighboring acceptor (PCBM) following photoexcitation[27,34,35]. The rapid GSB decay within 10 ps (seen in Fig 4(a)) is still a matter of debate and two possibilities have been proposed: (a) an exciton-charge annihilation quenching mechanism; and (b) the different bleaching cross-sections of the P3HT exciton and the polaron[27]. The weak SE peak at ~730 nm (seen at 1 ps delay, overlaid in the background of the strong PIA signal) indicates the presence of a small population of excitons photogenerated in the P3HT bulk (and away from the P3HT-PCBM interface) that decays within 10 ps. These observations agree with earlier findings of exciton quenching occurring rapidly (<10 ps) in intimately-blended P3HT:PCBM bulk heterojunction films[27].

Similar to the P3HT only samples, the magnitude of the DT signal for the 0-0 and 0-1 transitions are more pronounced in the NF Blend samples than the TA Blend samples of equivalent thicknesses (for 0-1 GSB signal, see Fig. S2 of Supporting Information). For the 0-0 transition, this is ~1.62 times larger

at the 1 ps onset. Nonetheless, the larger population of photogenerated charges (~62% more) in the NF Blend is consistent with the enhanced absorbance of the P3HT-NF films. At timescales between 100 ps – 2 ns, the GSB signals in both the TA Blend and NF Blend are almost invariant (see Fig. S2 of Supporting Information). For the 0-0, and 0-1 transitions within the time scales of 100 ps – 2 ns, the DT signal is about 62% and 21% larger, respectively in the NF Blend; consistent with a larger population of long-lived hole polarons in the NF Blend[27]. These observations agree with the earlier hypothesis that efficient exciton harvesting is not compromised in the NF system – i.e. charge separation laterally at the P3HT:PCBM interface around the width of the NF is indeed supported in the NF system. The near invariance of the GSB signal over the 100 ps – 2 ns time scale in Fig. 4(b) further indicates that the geminate recombination in both the ordered TA Blend and NF Blend samples are suppressed; in agreement with earlier reports[33,36,37]. Geminate recombination is a monomolecular process that occurs when two opposite charges originating from the same exciton (following dissociation) recombine and this process dominates the recombination dynamics at early times (hundreds of ps to few ns) in blend systems with low crystalline order (i.e. regio-random P3HT-PCBM blends). In contrast, non-geminate recombination is a bi-molecular process that occurs when two spatially separated charges recombine and this process dominates the recombination dynamics over the ns – μs timescale. To probe the dynamics of these long-lived charges at even longer time scales for the blend films, nanosecond laser flash photolysis spectroscopy was also performed.

3.3 Charge Carrier Dynamics in the ns-μs Temporal Regime

Fig. 5 shows the ns-transient absorption measurements for both the TA Blend and the NF Blend samples. In agreement with the earlier fs-TAS results, the magnitude of the DT signals at the 0-0 and 0-1 transitions in the NF Blend sample are indeed larger than that of TA Blend sample in the early ns timescale, a trend which extends to hundreds of ns (for 0-1 GSB signal, see Fig. S3 of Supporting

Information). For the 0-0 transition, this is ~1.6 times larger at the 2 ns onset; which corresponds well with the ratio obtained from the fs-TAS measurements. Beyond 100 ns, there is a rapid decrease in the GSB DT signals in the NF Blend sample that eventually matches the values of the TA Blend sample. This PB decay can be attributed to the non-geminate recombination (or bi-molecular recombination) process[22,38], where a rapid decrease in the DT signals (for the GSB bands) indicates a higher rate of non-geminate recombination in the NF Blend sample compared to the TA Blend sample. The normalized decay dynamics is available in Fig. S3(d) of Supporting Information for easy comparison.

Although the NF Blend possesses the advantage of higher absorbance and greater initial population of the photogenerated charges (compared to TA Blend), the non-geminate recombination process which is charge density dependent also becomes more pronounced in the NF Blend samples. One possibility for the more significant non-geminate recombination is the presence of considerable defects in the polymer which leads to charge trapping and causes higher charge concentrations. However, we have seen earlier from the small spectra redshift that charge trapping due to defects would be minimal in these ordered P3HT systems. Hence, we relate the significant non-geminate recombination in the NF Blend to arise from the poor inter-fibrillar charge transport instead. We infer that while there is high charge mobility along the nanofiber (i.e. in the direction of π-π stacking and along the polymer chain), the interconnected P3HT fibrillar network is still essentially a 2-D network where vertical transport to the electrodes has low charge mobility. Poor vertical inter-fibrillar transport between NFs which tend to lie parallel to the electrodes would give rise to charge localization. In the limit of charge trapping at the detached domains coupled with a higher initial density of photogenerated carriers, it is understandable that the non-geminate recombination rate is higher in the NF Blend sample, thereby competing with the charge extraction. Charge localization would also cause a redistribution of the local electric fields, thus impeding the charge extraction to the electrodes. These two factors would cause the

lowering of the FF of a PV device. The relevance of these fundamental processes to the device performance of these OPV cells will be discussed in a later section.

3.4 Modeling the Charge Carrier Recombination Dynamics

To gain a deeper physical insight into the dynamical processes in these blends, the analytical model developed by Laquai and co-workers was employed to analyze the branching ratios of geminate (monomolecular) versus non-geminate (bimolecular) recombination in these blends[39]. In their model, two populations comprising of (a) charge transfer (CT) states and (b) free charge carriers are believed to be formed following the dissociation of the singlet excitons. Unlike Laquai who fitted the dynamics over the spectral range of 750 – 850 nm, where the cross-sections of the CT states and the free charges are similar, we fitted the GSB 0-0 dynamics (i.e. at ~620 nm) using the model. In spite of the possibility of having dissimilar cross-sections, as a first approximation, these fits would still allow us to compare the relative fractions of the geminate and non-geminate recombination present in the NF Blend and the TA Blend. The rate equations describing the population dynamics are:

$$\frac{dCT}{dt} = -k_{CT\to GS}CT \qquad (1)$$

$$\frac{d(SSC)}{dt} = -\gamma SSC^{\lambda+1} \qquad (2)$$

$$\frac{dGS}{dt} = k_{CT\to GS}CT + \gamma SSC^{\lambda+1} \qquad (3)$$

while the solutions to this set of equations are:

$$CT(t) = N_0(1-f)\exp(-k_{CT\to GS}t) \qquad (4)$$

$$SSC(t) = \left(\lambda\gamma t + (fN_0)^{-\lambda}\right)^{-1/\lambda} \qquad (5)$$

$$GS(t) = N_0(1-f)\left(1-\left[\exp(-k_{CT\to GS}t)\right]\right) + N_0 f - \left(\lambda\gamma t + (fN_0)^{-\lambda}\right)^{-1/\lambda} \qquad (6)$$

where CT is the charge-transfer state population density, SSC is the spatially-separated charge population density, GS is the population relaxed to the ground state, $k_{CT\rightarrow GS}$ is the geminate recombination rate, γ is the density-dependent recombination rate constant, and λ+1 is the order of non-geminate recombination[33]. Determination of N_0, the initial excitation density is explained in the Supporting Information.

A representative plot of the fits is shown in Fig. 5. The parameters extracted from our best fit are shown in **Table 1**. The order of non-geminate recombination (λ) is equal to 1, in the case of 3D isotropic Langevin recombination with time- and density- independent mobility. However, from our fits, the value of λ is larger than 1, which is possible in the case where the morphology limits the diffusion or if the mobility is time- or charge-dependent[40]. The lower value of λ from our fit on NF Blend agrees with the earlier findings where λ has been observed to be lower in systems with a higher degree of ordering and more shallow traps[41]. The geminate recombination ($k_{CT\rightarrow GS}$) rates we obtained from our fits on TA and NF Blend are 1.0×10^8 1/s and 1.2×10^8 1/s, respectively. The similarity in the geminate recombination rates of the TA and NF Blend means that the morphology of the NF Blend is as effective as that of the TA Blend in assisting the geminate pairs at P3HT:PCBM interface dissociate to become free carriers.

An important finding that our fits reveal is that in the NF Blend, ~9% of the excitons generate interfacial charge transfer states that recombine by fast ns geminate recombination; while ~91% of excitons create free charge carriers on an ultrafast time scale that contribute to the extracted photocurrent. Comparatively, these values are ~14% and ~86% respectively in the control samples. These latter values for the TA Blend control samples correspond well with those reported by Laquai and co-workers (i.e. 15% (geminate) versus 85% (non-geminate) for the regio-regular P3HT:PCBM (annealed) samples). This finding validates our earlier deduction of better charge generation and polaron formation in the NF system. Despite the higher yield of free charges in the NF Blend, ns-transient

absorption spectroscopy also reveal that there is a higher rate of non-geminate recombination in the NF Blend sample compared to the control samples. Next we shall examine these findings from the modeling and those from the transient spectroscopy in relation to the device performance of these samples.

3.5 Device Performance

Table 2 shows a summary of the device performance parameters for the NA Blend, TA Blend and NF Blend devices. Samples possessing a higher degree of crystallinity and molecular ordering (i.e. the latter two) yield higher PCE values. This improvement is attributed to the enhanced photon absorbance and better phase separation of the P3HT and PCBM domains, leading to higher population of the photogenerated charges and a more efficient charge transport to the electrodes. From Fig. 6(a), both the TA Blend and NF Blend devices exhibit much larger J_{SC} and FF values compared to the pristine P3HT:PCBM. However, compared to the TA Blend devices, the NF Blend devices typically exhibit smaller but comparable J_{SC} and V_{OC} values. However, the FF is significantly smaller in the NF Blend devices than the TA Blend devices. Fig. 6(b) shows the spectral dependence of the EQE where the NF Blend devices generally exhibit a smaller value compared to the TA Blend samples across a broad spectral range with the former approaching 58% and the latter 66% at the absorption maximum of the polymer. This indicates that fewer charges were collected at the electrodes in the NF Blend devices. The significantly lower FF of the NF Blend devices compared to the TA Blend devices also shows that with a decreasing net electric field in the device, charge extraction becomes even less efficient. Previously, Laquai and co-workers have shown that the increased bias dependence of the photocurrent (i.e. corresponding to a decrease in FF) in a P3HT:PCBM blend is accounted for by the higher charge carrier densities that result in the bimolecular recombination competing with the charge extraction[39]. By studying the temperature and pump intensity dependence of the photocurrent, they also found that the

device properties were not governed by the charge-transfer state separation as previously perceived[42-44]. The principle conclusion was that the competition between the charge extraction and non-geminate recombination of free carriers strongly influence the bias dependence of the photocurrent.

Our findings from the device performance studies agrees with the findings from the optical spectroscopy presented in the earlier section where it was found that the NF Blend suffers from a higher rate of non-geminate recombination which eventually limits the amount of charge that is being collected by the electrode (see Fig. 5 and Fig. S3(d) in the Supporting Information). The poor vertical inter-fibrillar charge transport between nanofiber planes aligned parallel to the electrodes would give rise to charge localizations. We can further infer from these results that as the net electric field in the device is being switched off, the charges become even less mobile since the electric-field assisted hopping to the electrodes is being inhibited. Charge localization would also lead to a redistribution of the local electric fields that would further exacerbate the situation (of poor charge extraction) as the device approaches the flat band conditions. This inevitably results in a smaller J_{SC} and FF for the NF Blend devices. Lastly, the greater degree of ordering in the P3HT-NF system also raises the HOMO level of the P3HT-NF system such that the energy gap which defines the V_{OC} of the system (i.e. between the between HOMO of P3HT and LUMO of PCBM) becomes smaller[10,45,46]. The raising of the HOMO level of P3HT with increasing crystallinity results in the decreasing of the V_{OC}, which is evident from the decreasing V_{OC} values of the pristine, annealed, and nanofiber P3HT:PCBM. Consequently, an interplay of all these factors influencing the J_{SC}, FF and V_{OC} inadvertently contribute to the smaller PCE for the NF Blend devices as compared to the nanoscale phase-separated TA Blend devices.

4. CONCLUSIONS

In summary, we have performed a systematic optical spectroscopy study on the charge generation and recombination dynamics in P3HT:PCBM blend films containing highly crystalline, interconnected P3HT-NF networks. TAS spanning a wide temporal range over 7 orders of magnitude (i.e. from 100 fs to 1 μs) was employed in this study and the relevance of these fundamental processes to the device performance of these OPV cells were correlated and discussed. fs-TAS reveals a more pronounced GSB signature persisting up to 2 ns in the NF Blend than that of the TA-Blend control. This indicates better charge generation and polaron formation in the NF system – a finding that is validated by the results of the modeling where a branching ratio of ~91% free charge carriers to ~9% CT states were obtained for the NF Blend compared to ~86% free charge carriers to ~14% CT states for the TA Blend. However, there is also a significant amount of non-geminate recombination in the NF system over the ns to μs timescale. We attribute this to the poor vertical inter-fibrillar transport between NFs aligned parallel to the electrodes, which results in charge localization and a higher density of carriers. This leads to a higher rate of bi-molecular recombination. Device performance studies reveal a significantly lower FF in the NF Blend devices compared to the TA Blend devices; indicating that charge extraction becomes less efficient with a decreasing net electric field in the former devices due to the inhibition of the electric-field assisted hopping and charge localizations, thus causing a redistribution of local electric fields. These findings from the device performance[8] studies concur with the findings from optical spectroscopy. Although the P3HT NF system possesses several salient advantages over their thermally annealed counterparts (i.e. thermal free post-processing compatible with plastic substrates and more efficient initial charge generation and polaron formation), the charge extraction issue encountered needs to be addressed in order to realize high efficiency polymer-nanofiber:fullerene solar cells. This may well be achieved through the fabrication of a vertically aligned P3HT NFs network

that is orthogonal to the electrodes to leverage on the high mobility intra-fibrillar charge transport properties whilst overcoming the limitation of poor inter-fibrillar charge transport.

ACKNOWLEDGEMENT- The authors would like to thank Prof Cesare Soci (Nanyang Technological University) for the fruitful discussions. The authors are also very grateful to Dr Frédéric Laquai (Max Planck Institute for Polymer Research) for the fruitful discussions on the analytical modeling. This work is supported by the following research grants: NTU start-up grant M4080514.110 NTU (M58110068); Academic Research Funds (AcRF) Tier 1 grants – M4010802.110 RG49/08 (M52110082) and M4010808.110 RG 55/08 (M52110088). T. C. S also acknowledges the financial support by the Singapore National Research Foundation (NRF) through the Competitive Research Programme (CRP) under Project No. NRF-CRP5-2009-04.

SUPPORTING INFORMATION AVAILABLE: Transient absorption spectra for TA P3HT, TA Blend, decay dynamics of TA P3HT, NF P3HT, TA Blend, and NF Blend, and a full list of references can be found in the supporting information. This information is available free of charge via the internet at http://pubs.acs.org.

FIGURES

Fig. 1

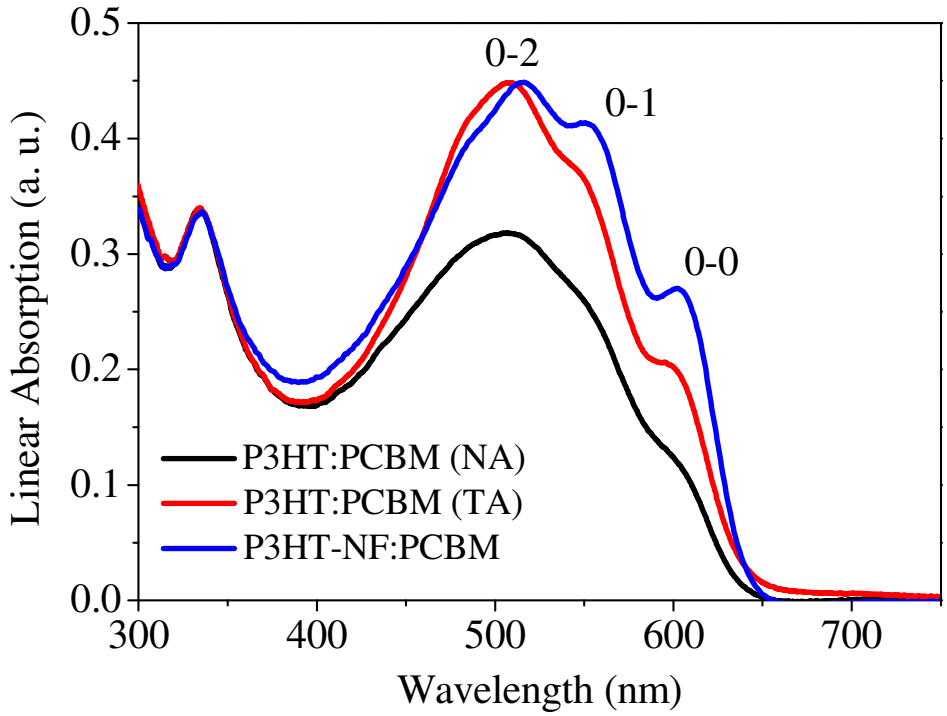

Fig 1. Linear absorption spectra of the pristine non-annealed P3HT:PCBM (NA Blend), thermal-annealed P3HT:PCBM (TA Blend) and non-annealed P3HT-NF:PCBM (NF Blend). The 340 nm peak is due to PCBM absorption.

Fig . 2

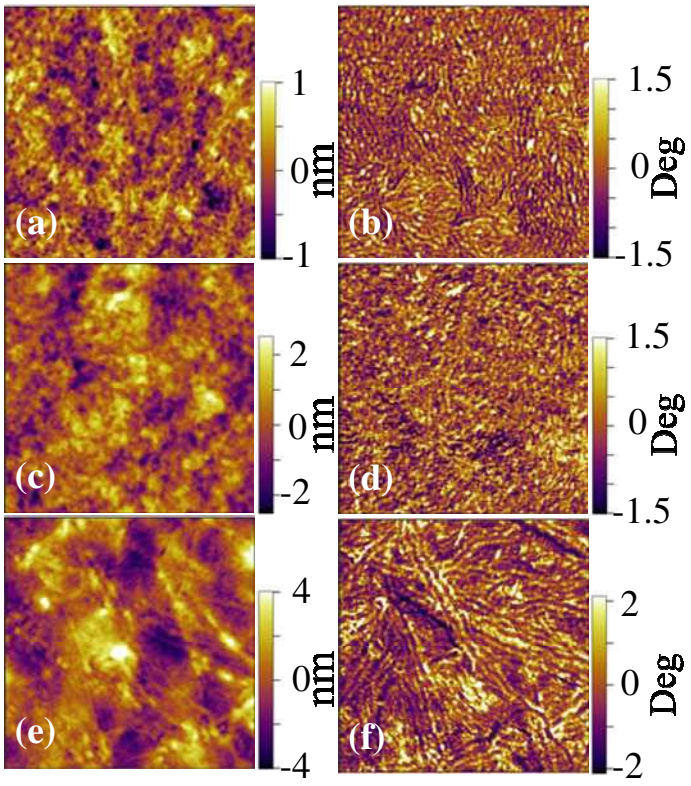

Fig 2. AFM scans of the surface topography of pristine P3HT:PCBM **(a)**, thermal-annealed P3HT:PCBM **(c)**, and nanofiber-P3HT:PCBM **(e)** and their corresponding phase images **(b)**, **(d)** and **(f)**. The scan area is 1 μm^2 for all images.

Fig . 3

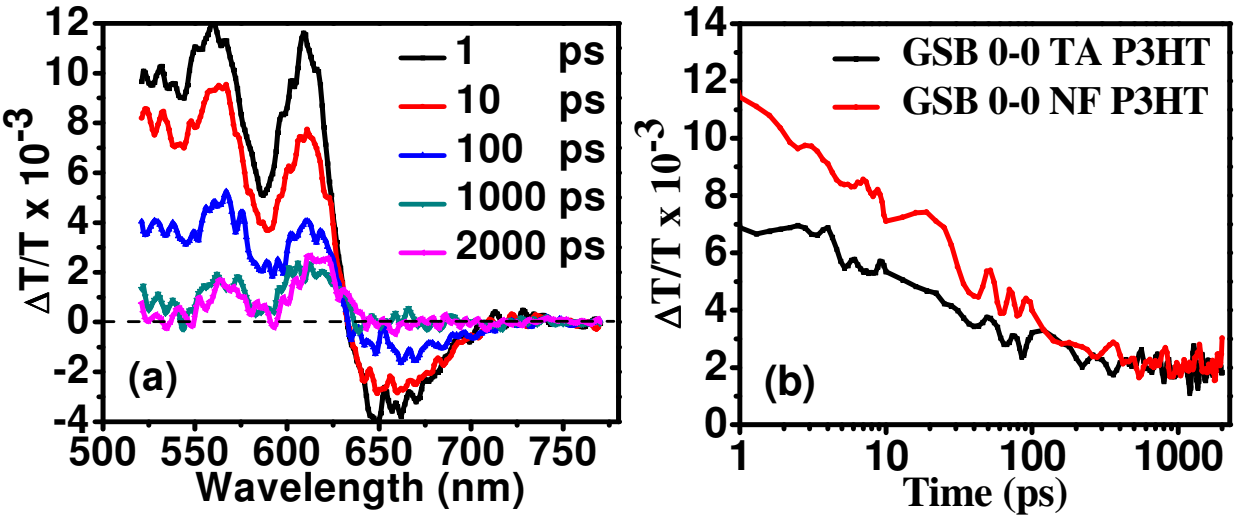

Fig 3. **(a)** fs-transient absorption spectra of NF P3HT. **(b)** The dynamics of the 0-0 GSB peak of TA P3HT and NF P3HT. For GSB 0-1 and GSB 0-2 dynamics, see **Supporting Information**.

Fig 4.

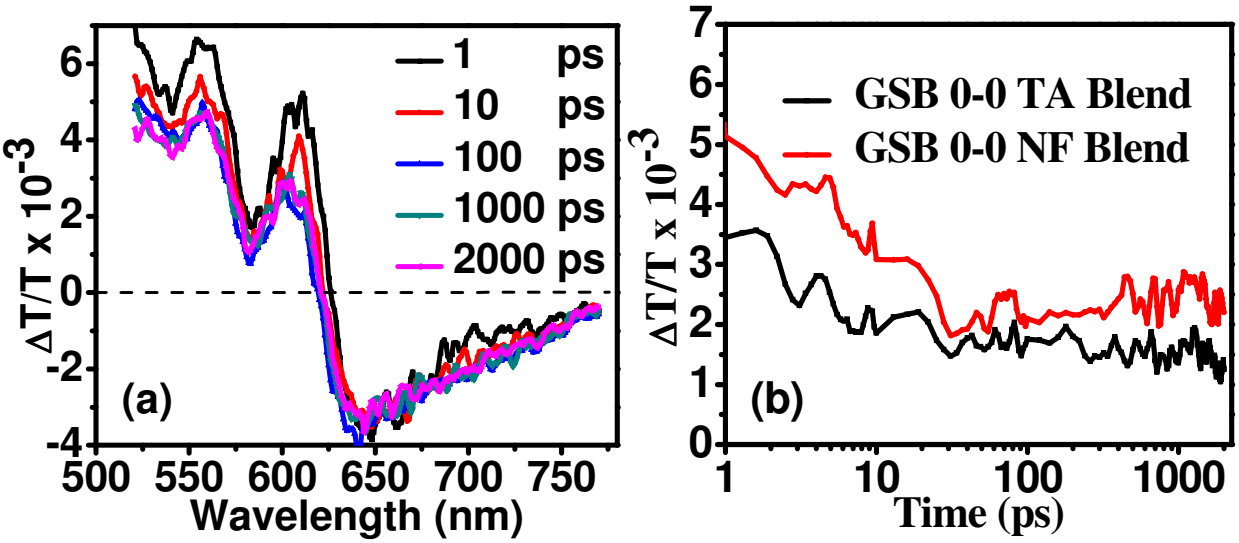

Fig 4. **(a)** fs-Transient absorption spectra of P3HT-nanofiber:PCBM (NF Blend). **(b)** The dynamics of the 0-0 GSB peak of TA Blend and NF Blend. For GSB 0-1 and GSB 0-2 dynamics, see **Supporting Information**.

Fig 5.

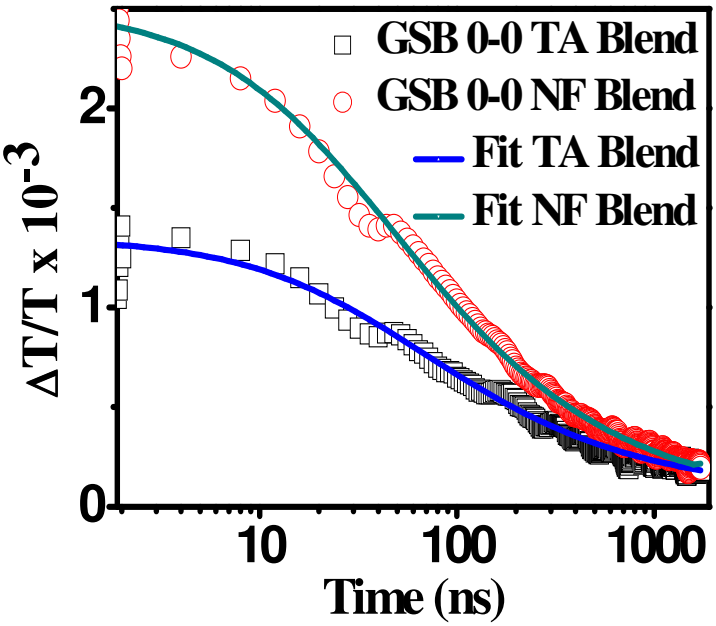

Fig 5. ns-Transient absorption decay dynamics of TA Blend and NF Blend in the ns – μs time scale. The dynamics of the 0-0 GSB peak of TA Blend and NF Blend, and fits to the GSB 0-0 decay dynamics using the analytical model of charge recombination are shown. For GSB 0-1 and GSB 0-2 dynamics, and Normalized ns-Transient absorption GSB 0-0 decay dynamics of TA Blend and NF Blend, see **Supporting Information**.

Fig 6.

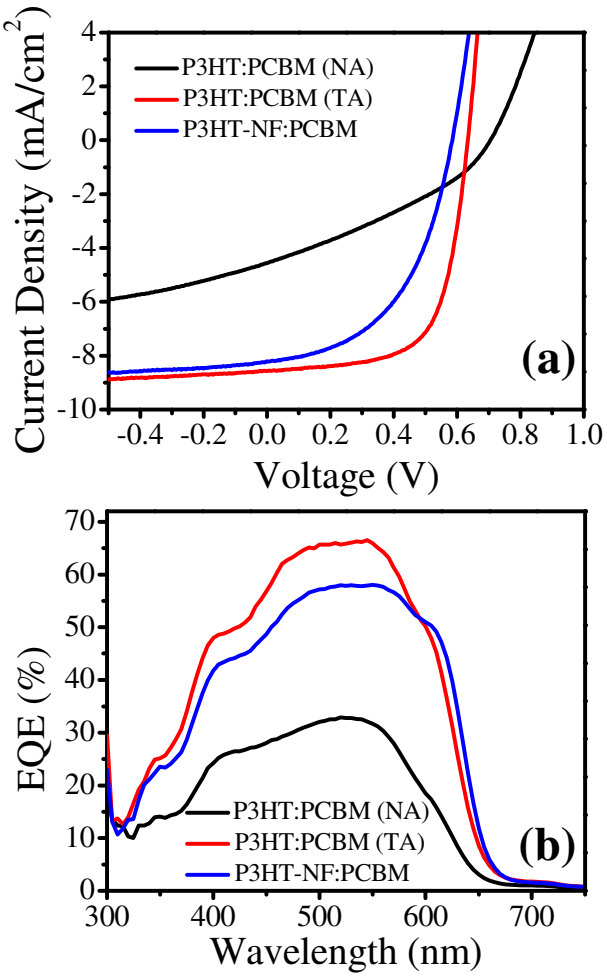

Fig 6. (a) *J*-V characteristics of devices fabricated with pristine, thermal-annealed P3HT:PCBM, and P3HT-NF:PCBM materials. **(b)** EQE measurements of the three devices.

Table 1.: Parameters extracted from the fitting of the GSB decay dynamics of TA Blend and NF Blend.

Parameter	TA Blend	NF Blend	rr-P3HT:PCBM (annealed) [ref 33]
1-f (fraction monomolecular recombination)	0.14 ± 0.03	0.09 ± 0.03	0.15 ± 0.01
f (fraction nongeminate recombination)	0.86 ± 0.03	0.91 ± 0.03	0.85 ± 0.01
$k_{CT \searrow GS}$ 1/s (geminate recombination rate)	$(1.0 \pm 0.3) \times 10^{8}$	$(1.2 \pm 0.3) \times 10^{8}$	$(2.5 \pm 0.2) \times 10^{8}$
λ+1 (order of non-geminate decay)	2.9 ± 0.1	2.6 ± 0.1	2.45 ± 0.01
γ $(cm^3)^{\lambda}$ s^{-1} (non-geminate decay rate)	$(6.3 \pm 0.9) \times 10^{-19}$	$(1.9 \pm 0.6) \times 10^{-19}$	$(1.9 \pm 0.3) \times 10^{-20}$

Table 2.: A summary of the performance of various devices. (Note the presence of some degree molecular ordering in the P3HT:PCBM (NA) samples and the device performance of these samples are included for completeness)

Sample	PCE (%)	J_{SC} ($^{mA}/_{cm^2}$)	V_{OC} (V)	FF
P3HT:PCBM (NA)	1.08	4.56	0.70	0.33
P3HT:PCBM (TA)	3.57	8.57	0.63	0.66
P3HT-NF:PCBM	2.40	8.21	0.58	0.50

REFERENCES

(1) Benanti, T. L.; Venkataraman, D. *Photosynth. Res.* **2006**, *87*, 73-81.
(2) Dennler, G.; Scharber, M. C.; Brabec, C. J. *Adv. Mater.* **2009**, *21*, 1323-1338.
(3) Hoppe, H.; Sariciftci, N. S. *J. Mater. Res.* **2004**, *19*, 1924-1945.
(4) Li, G.; Shrotriya, V.; Huang, J. S.; Yao, Y.; Moriarty, T.; Emery, K.; Yang, Y. *Nat. Mater.* **2005**, *4*, 864-868.
(5) Moule, A. J.; Meerholz, K. *Adv. Funct. Mater.* **2009**, *19*, 3028-3036.
(6) Nelson, J. *Curr. Opin. Solid State. Mater. Sci.* **2002**, *6*, 87-95.
(7) Kim, J. Y.; Kim, S. H.; Lee, H. H.; Lee, K.; Ma, W. L.; Gong, X.; Heeger, A. J. *Adv. Mater.* **2006**, *18*, 572-576.
(8) Li, G.; Shrotriya, V.; Yao, Y.; Yang, Y. *J. Appl. Phys.* **2005**, *98,* 043704.
(9) Ma, W. L.; Yang, C. Y.; Gong, X.; Lee, K.; Heeger, A. J. *Adv. Funct. Mater.* **2005**, *15*, 1617-1622.
(10) Reyes-Reyes, M.; Kim, K.; Carroll, D. L. *Appl. Phys. Lett.* **2005**, *87*, 083506.
(11) Guo, J. M.; Ohkita, H.; Benten, H.; Ito, S. *J. Am. Chem. Soc.* **2010**, *132*, 6154-6164.
(12) Li, G.; Yao, Y.; Yang, H.; Shrotriya, V.; Yang, G.; Yang, Y. *Adv. Funct. Mater.* **2007**, *17*, 1636-1644.
(13) Park, J. H.; Kim, J. S.; Lee, J. H.; Lee, W. H.; Cho, K. *J. Phys. Chem. C* **2009**, *113*, 17579-17584.
(14) Yang, X.; Loos, J. *Macromolecules* **2007**, *40*, 1353-1362.
(15) Zhao, G. J.; He, Y. J.; Li, Y. F. *Adv. Mater.* **2010**, *22*, 4355-4358.
(16) Kim, J. S.; Park, Y.; Lee, D. Y.; Lee, J. H.; Park, J. H.; Kim, J. K.; Cho, K. *Adv. Funct. Mater.* **2010**, *20*, 540-545.
(17) Kim, J. H.; Park, J. H.; Lee, J. H.; Kim, J. S.; Sim, M.; Shim, C.; Cho, K. *J. Mater. Chem.* **2010**, *20*, 7398-7405.
(18) Kim, J. S.; Lee, J. H.; Park, J. H.; Shim, C.; Sim, M.; Cho, K. *Adv. Funct. Mater.* **2011**, *21*, 480-486.
(19) Sun, S. Y.; Salim, T.; Wong, L. H.; Foo, Y. L.; Boey, F.; Lam, Y. M. *J. Mater. Chem.* **2011**, *21*, 377-386.
(20) Moon, J. S.; Lee, J. K.; Cho, S. N.; Byun, J. Y.; Heeger, A. J. *Nano Lett.* **2009**, *9*, 230-234.
(21) van Bavel, S. S.; Sourty, E.; de With, G.; Loos, J. *Nano Lett.* **2009**, *9*, 507-513.
(22) Berson, S.; De Bettignies, R.; Bailly, S.; Guillerez, S. *Adv. Funct. Mater.* **2007**, *17*, 1377-1384.
(23) Kim, Y.; Cook, S.; Tuladhar, S. M.; Choulis, S. A.; Nelson, J.; Durrant, J. R.; Bradley, D. D. C.; Giles, M.; McCulloch, I.; Ha, C. S. et al. *Nat. Mater.* **2006**, *5*, 197-203.
(24) Li, L. G.; Lu, G. H.; Yang, X. N. *J. Mater. Chem.* **2008**, *18*, 1984-1990.
(25) Salim, T.; Sun, S. Y.; Wong, L. H.; Xi, L. F.; Foo, Y. L.; Lam, Y. M. *J. Phys. Chem. C* **2010**, *114*, 9459-9468.
(26) Guo, J. M.; Ohkita, H.; Benten, H.; Ito, S. *J. Am. Chem. Soc.* **2009**, *131*, 16869-16880.
(27) Marsh, R. A.; Hodgkiss, J. M.; Albert-Seifried, S.; Friend, R. H. *Nano Lett.* **2010**, *10*, 923-930.
(28) Shuttle, C. G.; O'Regan, B.; Ballantyne, A. M.; Nelson, J.; Bradley, D. D. C.; de Mello, J.; Durrant, J. R. *Appl. Phys. Lett.* **2008**, *92*, 093311.
(29) Clark, J.; Silva, C.; Friend, R. H.; Spano, F. C. *Phys. Rev. Lett.* **2007**, *98*, 206406.

(30) Spano, F. C. *J. Chem. Phys.* **2005**, *122*, 234701.
(31) Cook, S.; Furube, A.; Katoh, R. *Eng. Env. Sci.* **2008**, *1*, 294-299.
(32) Cook, S.; Han, L. Y.; Furube, A.; Katoh, R. *J. Phys. Chem. C* **2010**, *114*, 10962-10968.
(33) Howard, I. A.; Mauer, R.; Meister, M.; Laquai, F. *J. Am. Chem. Soc.* **2010**, *132*, 14866-14876.
(34) Xie, Y.; Li, Y.; Xiao, L. X.; Qiao, Q. Q.; Dhakal, R.; Zhang, Z. L.; Gong, Q. H.; Galipeau, D.; Yan, X. Z. *J. Phys. Chem. C* **2010**, *114*, 14590-14600.
(35) Bredas, J. L.; Norton, J. E.; Cornil, J.; Coropceanu, V. *Acc. Chem. Res.* **2009**, *42*, 1691-1699.
(36) Shuttle, C. G.; O'Regan, B.; Ballantyne, A. M.; Nelson, J.; Bradley, D. D. C.; Durrant, J. R. *Phys. Rev. B* **2008**, *78*, 113201.
(37) Thompson, B. C.; Frechet, J. M. J. *Angew. Chem. Int. Ed.* **2008**, *47*, 58-77.
(38) Ohkita, H.; Cook, S.; Astuti, Y.; Duffy, W.; Tierney, S.; Zhang, W.; Heeney, M.; McCulloch, I.; Nelson, J.; Bradley, D. D. C. et al. *J. Am. Chem. Soc.* **2008**, *130*, 3030-3042.
(39) Mauer, R.; Howard, I. A.; Laquai, F. *J. Phys. Chem. Lett.* **2010**, *1*, 3500-3505.
(40) Shuttle, C. G.; Hamilton, R.; Nelson, J.; O'Regan, B. C.; Durrant, J. R. *Adv. Funct. Mater.* **2010**, *20*, 698-702.
(41) Clarke, T. M.; Jamieson, F. C.; Durrant, J. R. *J. Phys. Chem. C* **2009**, *113*, 20934-20941.
(42) De, S.; Pascher, T.; Maiti, M.; Jespersen, K. G.; Kesti, T.; Zhang, F. L.; Inganas, O.; Yartsev, A.; Sundstrom, V. *J. Am. Chem. Soc.* **2007**, *129*, 8466-8472.
(43) Mihailetchi, V. D.; Koster, L. J. A.; Hummelen, J. C.; Blom, P. W. M. *Phys. Rev. Lett.* **2004**, *93*, 216601.
(44) Veldman, D.; Ipek, O.; Meskers, S. C. J.; Sweelssen, J.; Koetse, M. M.; Veenstra, S. C.; Kroon, J. M.; van Bavel, S. S.; Loos, J.; Janssen, R. A. J. *J. Am. Chem. Soc.* **2008**, *130*, 7721-7735.
(45) Vandewal, K.; Gadisa, A.; Oosterbaan, W. D.; Bertho, S.; Banishoeib, F.; Van Severen, I.; Lutsen, L.; Cleij, T. J.; Vanderzande, D.; Manca, J. V. *Adv. Funct. Mater.* **2008**, *18*, 2064-2070.
(46) Vanlaeke, P.; Swinnen, A.; Haeldermans, I.; Vanhoyland, G.; Aernouts, T.; Cheyns, D.; Deibel, C.; D'Haen, J.; Heremans, P.; Poortmans, J. et al. *Sol. Eng. Mater. Sol. Cells* **2006**, *90*, 2150-2158.

TOC Image

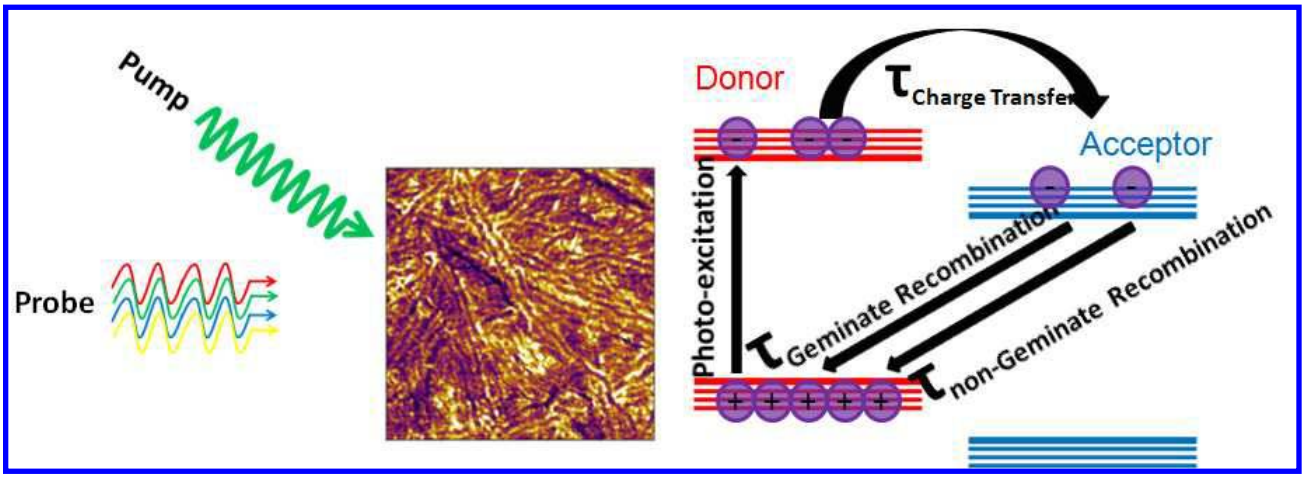
Pump
Probe
Donor
τ Charge Transfer
Acceptor
Photo-excitation
τ Geminate Recombination
τ non-Geminate Recombination

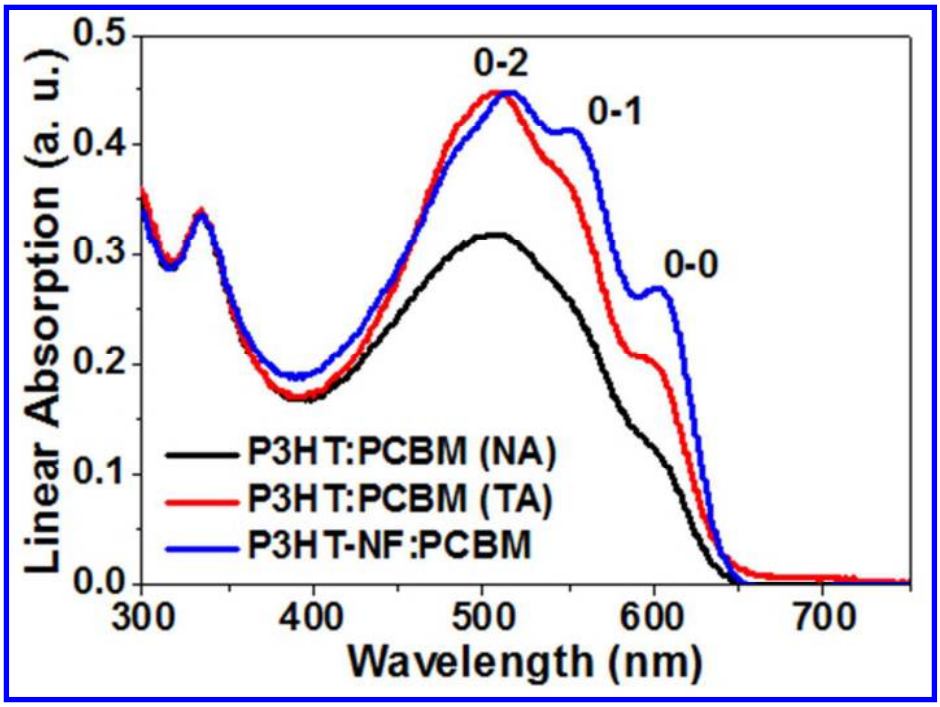

161x120mm (72 x 72 DPI)

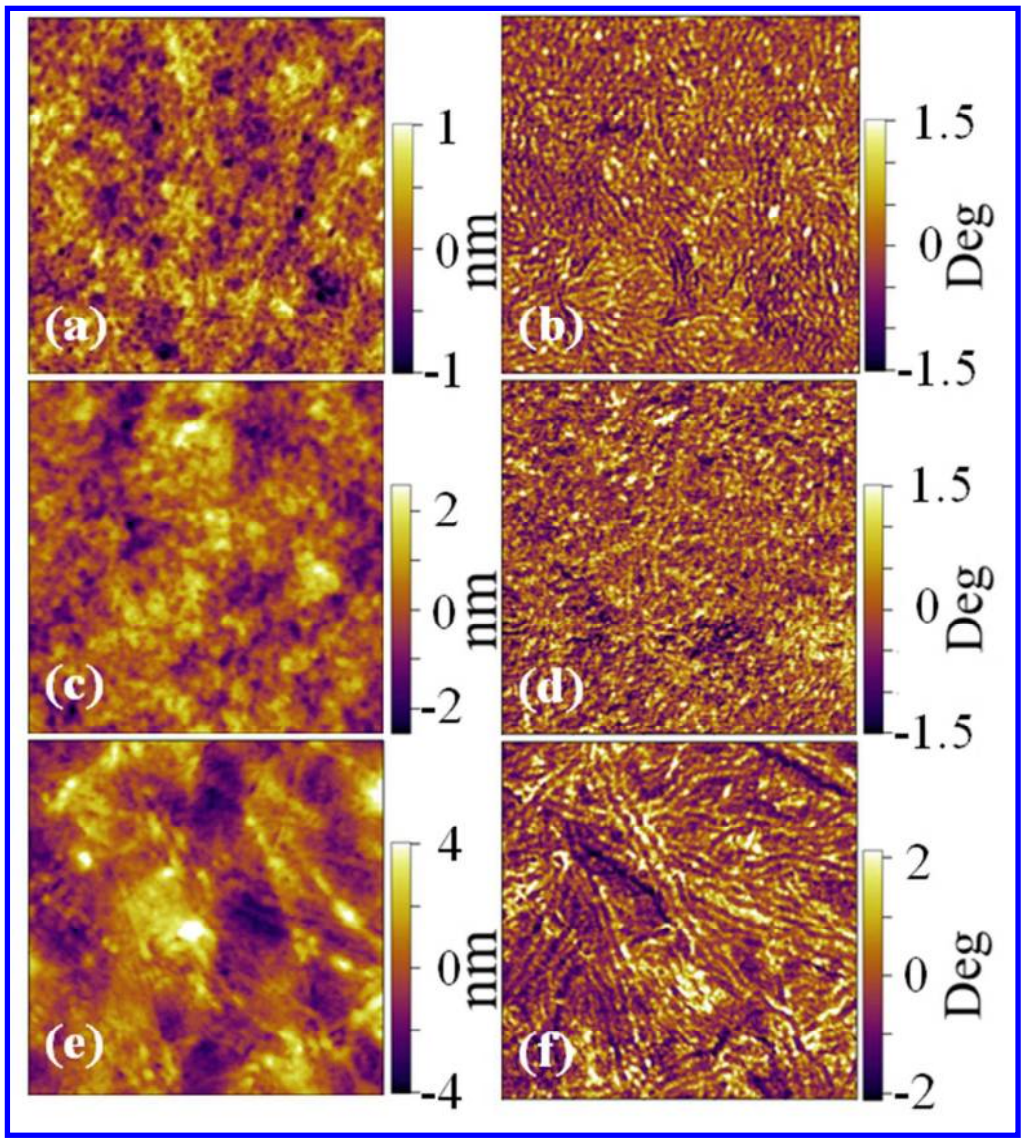

212x238mm (72 x 72 DPI)

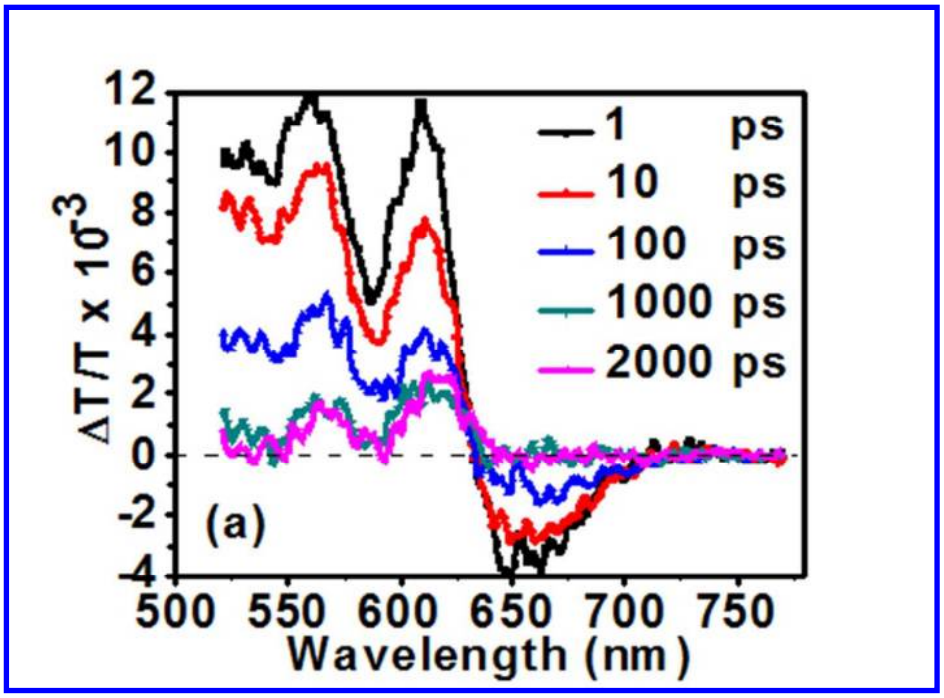

162x118mm (72 x 72 DPI)

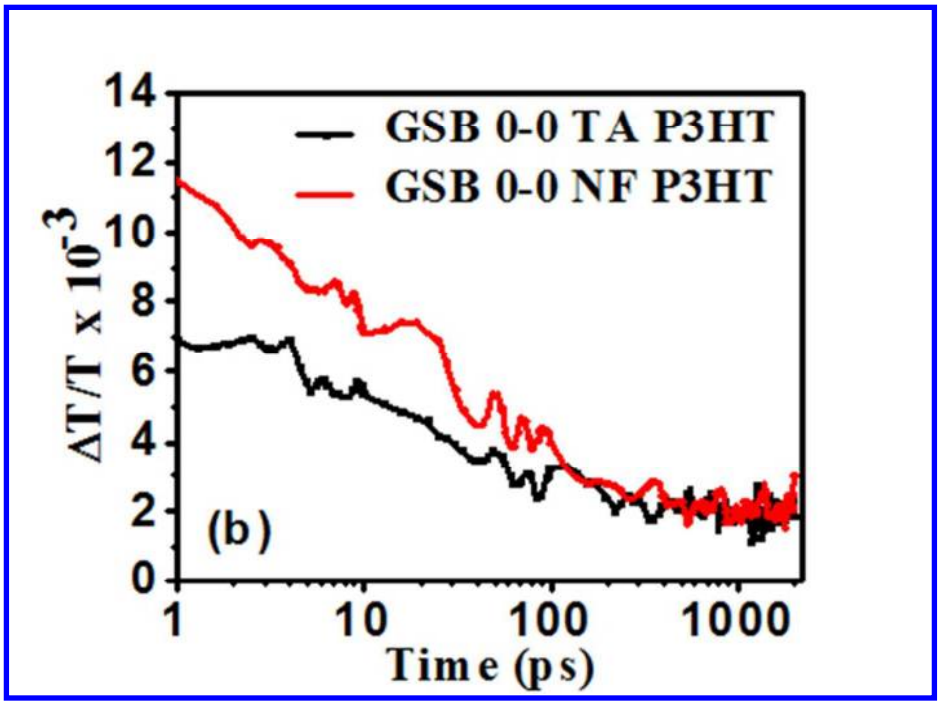

161x119mm (72 x 72 DPI)

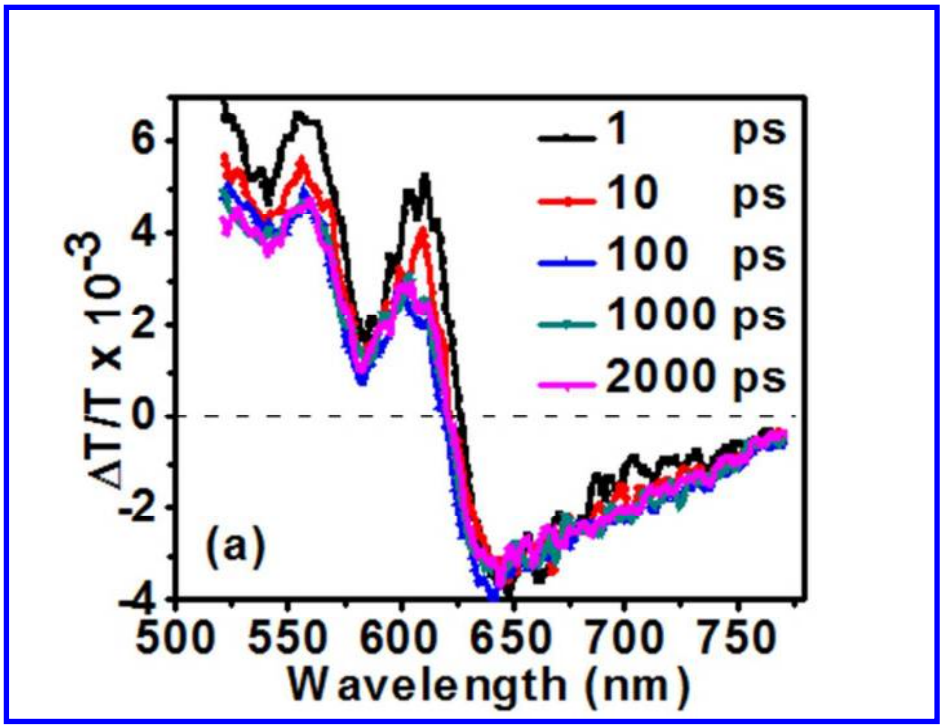

162x124mm (72 x 72 DPI)

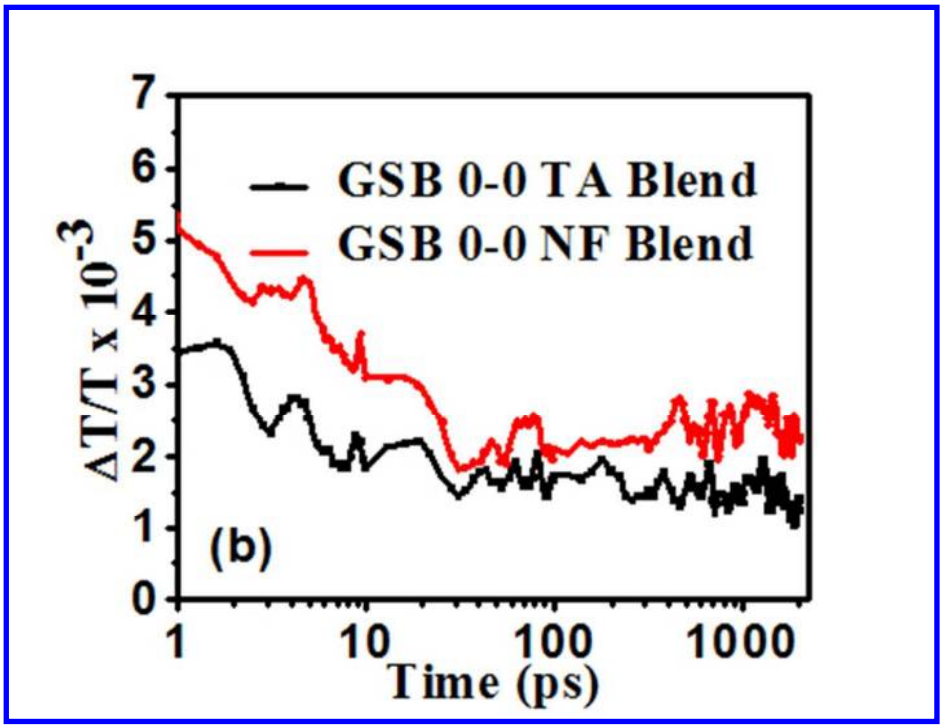

162x124mm (72 x 72 DPI)

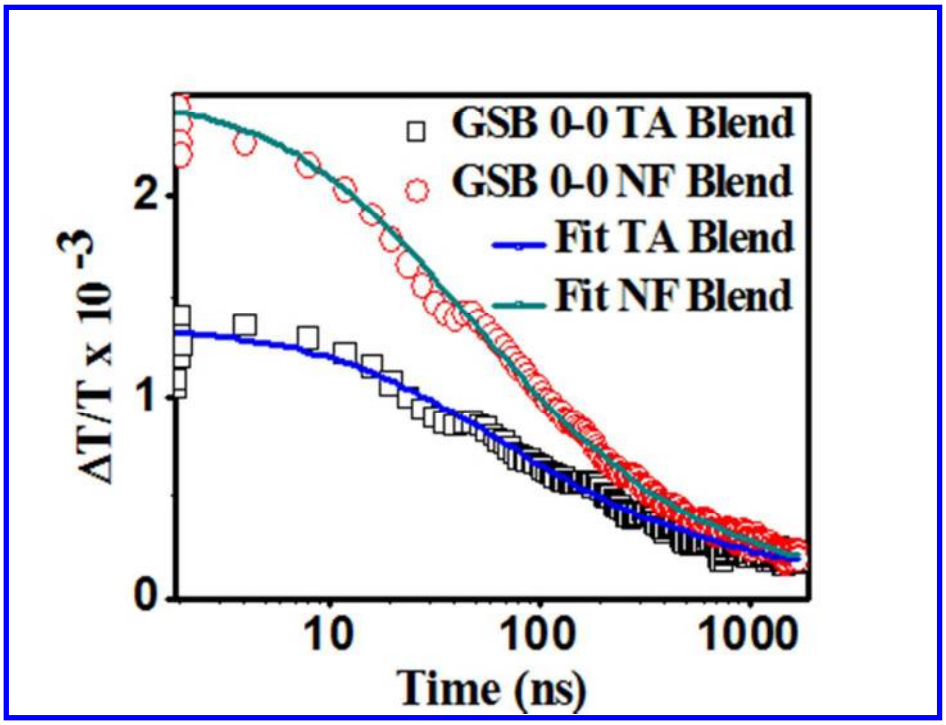

162x123mm (72 x 72 DPI)

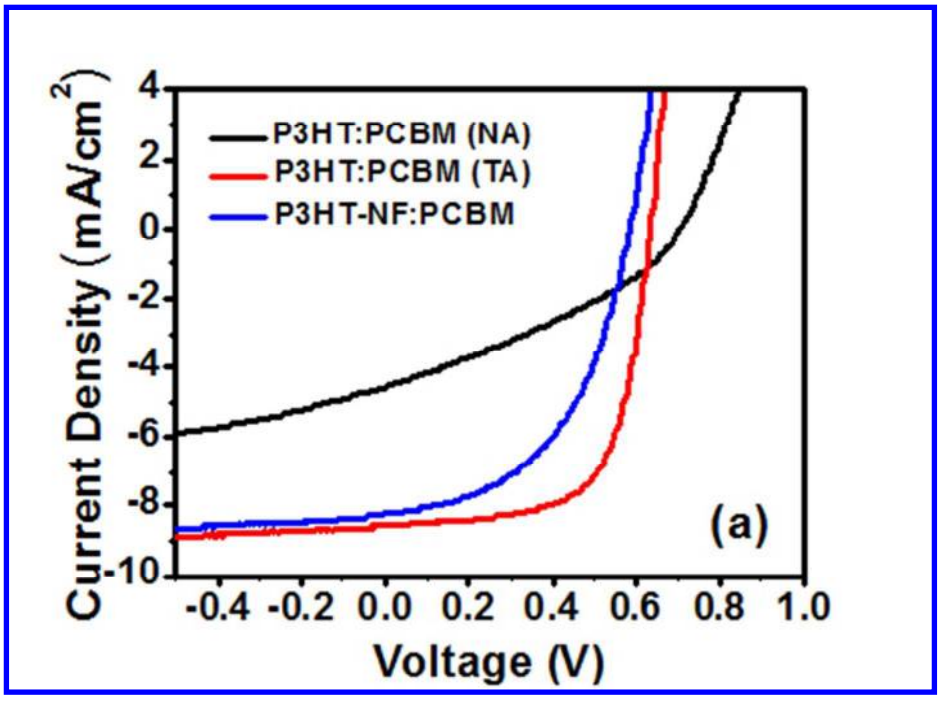

161x119mm (72 x 72 DPI)

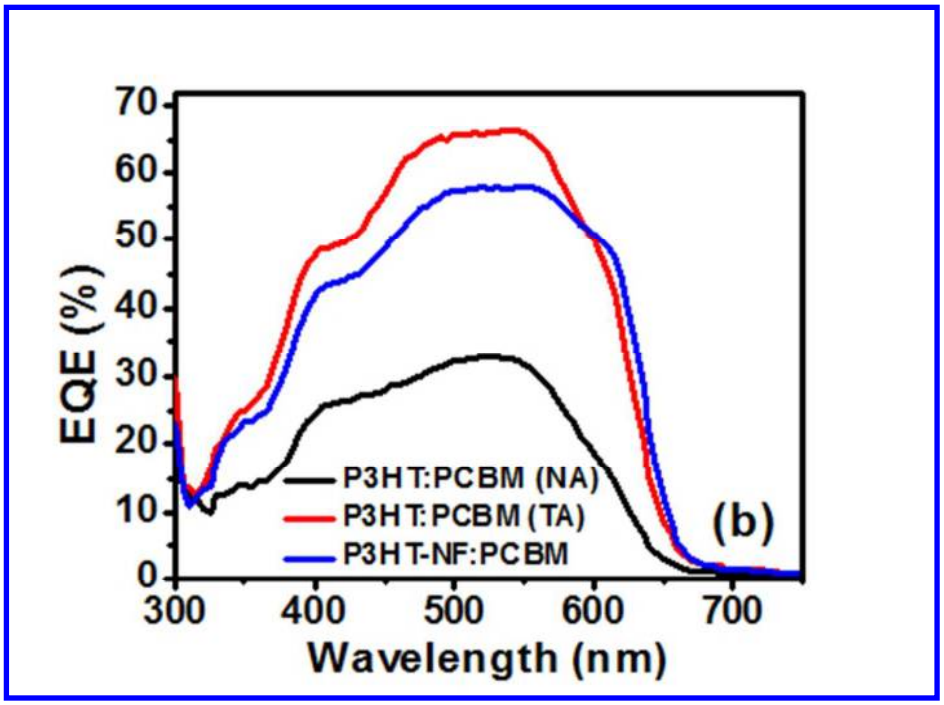

162x119mm (72 x 72 DPI)

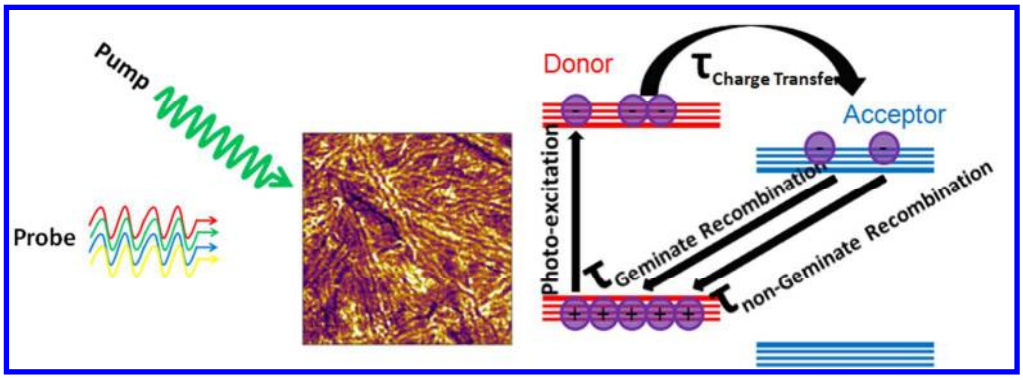

323x114mm (72 x 72 DPI)